



# Noninvasive OCT angiography-based blood attenuation measurements correlate with blood glucose level in the mouse retina

KAIYUAN LIU,<sup>1</sup> TIEPEI ZHU,<sup>2</sup> LIN YAO,<sup>1</sup> ZIYI ZHANG,<sup>1</sup> HUAKUN LI,<sup>1</sup> JUAN YE,<sup>2</sup> AND PENG LI<sup>1,3,4,\*</sup> 

<sup>1</sup>State Key Lab of Modern Optical Instrumentation, College of Optical Science and Engineering, Zhejiang University, Hangzhou, Zhejiang 310027, China

<sup>2</sup>Eye Center of the Second Affiliated Hospital, College of Medicine, Zhejiang University, Hangzhou, Zhejiang 310003, China

<sup>3</sup>Hebei Key Laboratory of Micro-Nano Precision Optical Sensing and Measurement Technology, Qinhuangdao, Hebei 066004, China

<sup>4</sup>International Research Center for Advanced Photonics, Zhejiang University, Hangzhou, Zhejiang 310027, China

\*peng\_li@zju.edu.cn

**Abstract:** In this study, we investigated the correlation of the blood optical attenuation coefficient (OAC) and the blood glucose concentration (BGC). The blood OAC was measured in mouse retina in vivo by analyzing the depth attenuation of backscattered light under the guidance of OCT angiography (OCTA) vascular mapping, and then its correlation to the BGC was further investigated. The optical attenuation of the blood components presented a more reliable correlation to BGC than that of the background tissues. The arteries and veins presented a blood OAC change of  $\sim 0.05\text{--}0.07\text{ mm}^{-1}$  per 10 mg/dl and a significant ( $P < 0.001$ ) elevation of blood OAC in diabetic mice was observed. Furthermore, different kinds of vessels also presented different performances. The veins had a higher correlation coefficient ( $R=0.86$ ) between the measured blood OAC and BGC than that of the arteries ( $R=0.73$ ). Besides, the blood OAC changes of the specific vessels occur without any obvious change in the vascular morphology in the retina. The blood OAC-BGC correlation suggests a concept of non-invasive OCTA-based glucometry, allowing a fast assessment of the blood glucose of specific vessels with superior motion immunity. A direct glucometry of the retina would be helpful for accurately monitoring the progression of diabetic retinopathy.

© 2021 Optical Society of America under the terms of the [OSA Open Access Publishing Agreement](#)

## 1. Introduction

Diabetes mellitus is a chronic metabolic disorder characterized by abnormal blood glucose level [1,2]. According to the International Diabetes Federation, about 463 million people were living with diabetes (DB) in 2019, and this number will reach 700 million by 2045 if this trend continues [3]. Control of this disease includes daily self-monitoring of blood glucose by taking blood samples with a finger puncture for chemical analysis. However, invasive monitoring leads to poor patient compliance and disease management. Significant efforts have been devoted to develop noninvasive techniques for monitoring blood glucose concentration (BGC), and various optical approaches were proposed to achieve this goal [4,5], including near-infrared absorption and scattering, polarimetry and Raman spectroscopy, but they have limited sensitivity, accuracy and specificity of BGC measurements.

There exists a physical correlation between the tissue optical scattering and glucose concentration [6–8]. Optical coherence tomography (OCT) allows a volumetric imaging of the internal microstructure in biological tissue by measuring the echoes of backscattered light of scatterers [9]. The optical attenuation coefficient (OAC) of the tissues can be extracted from the OCT depth

profile which reveals the attenuation of the backscattering signal versus the depth [10–12]. The measured OAC is mainly contributed by the tissue scattering which is substantially larger than absorption in the near-infrared spectral range [13]. The OAC of the lower dermis was precisely measured without unwanted signal from the epidermis and upper dermis in human skin [13,14], and the OAC decreases in response to a growing of glucose level, which is most likely due to the reduced refractive index (RI) mismatch between the interstitial fluid and cell membranes [15]. The OAC-Glucose correlation allows a noninvasive monitoring of glucose concentration with OCT (OCT-G). However, the skin tissue is highly inhomogeneous with non-uniform density and RI distribution in space, and changing the imaging site (e.g. tissue motion) would induce huge fluctuations of OAC [13], severely limiting its applications in practice.

Comparatively, the blood component, which mainly consists of plasma and erythrocytes, is spatially homogeneous, and a high blood optical attenuation coefficient (OAC)-Glucose relation was also observed in vitro in the whole blood samples [16]. In addition, OCT angiography (OCTA), a functional extension of OCT structural imaging, allows a mapping of vasculature within the tissue bed [17–20]. Under the guidance of the OCTA vascular mapping, the blood OAC of specific vessels can be measured directly in vivo, and the averaged blood OAC of specific vessels potentially enables a fast assessment of the blood glucose with a high immunity to the tissue motion.

In this study, the blood OAC of specific vessels was measured in mouse retina in vivo by analyzing the OCT depth profile under the guidance of OCTA vascular mapping. We demonstrate the averaged blood OAC of arteries and veins has a high correlation to the BGC and a significant difference of blood OAC exists between the control and DB groups in mouse retina. The differences of blood OAC between the retinal arteries and veins were further discussed. The obtained blood OAC-BGC correlation suggests a concept of non-invasive OCTA-based glucometry (OCTA-G) which has the superiorities: 1) the capability of assessing the glucose of specific vessels enabled by OCTA; 2) the motion immunity in glucose assessment attributed by the homogeneity of blood.

## 2. Materials and methods

### 2.1. OCTA setup and scanning protocol

A lab-built spectral domain OCTA system (see Fig. 1) was used in this study for in vivo imaging of mouse retina. A broadband super luminescent diode (Superlum, Ireland) with a central wavelength of 840 nm and a spectral bandwidth of 100 nm was used as the light source, providing a measured axial resolution of  $\sim 4\ \mu\text{m}$  (the full-width at half maximum of interference peak) in air. The output light was delivered into a fiber coupler and split into the sample and reference arms. In the sample arm, a set of galvanometer scanners and an ocular lens were adopted to realize two-dimensional (2D) scanning in x-y directions and achieve a lateral resolution of  $\sim 10\ \mu\text{m}$  in the mouse retina. A high-speed spectrometer equipped with a fast line-scan camera (e2v, UK) was used to record the interference fringes, providing 100 kHz line-scan rate with 2048 active pixels.

In this study, a stepwise raster scanning protocol (z-x-y) was used for volumetric imaging, with 400 A-lines per B-scan (fast-scan, x direction) and 1200 B-scans repeated 3 times at 400 tomographic positions per volume (slow-scan, y direction). Each volumetric scan was completed within 6 s and covered a field of view (FOV) of  $\sim 2\ \text{mm} \times 2\ \text{mm}$  (x-y) centered on the optic nerve head of mouse retina.

### 2.2. Animal preparation

All experiments were conducted on 10-12 weeks old male C57BL/6J mice, including control group ( $n = 10$ , weight  $21.28 \pm 2.29\ \text{g}$ ) and streptozotocin DB group ( $n = 10$ , weight  $22.03 \pm 2.20\ \text{g}$ ), both of which were obtained from Zhejiang Medical Science Institute. Before OCTA scan,

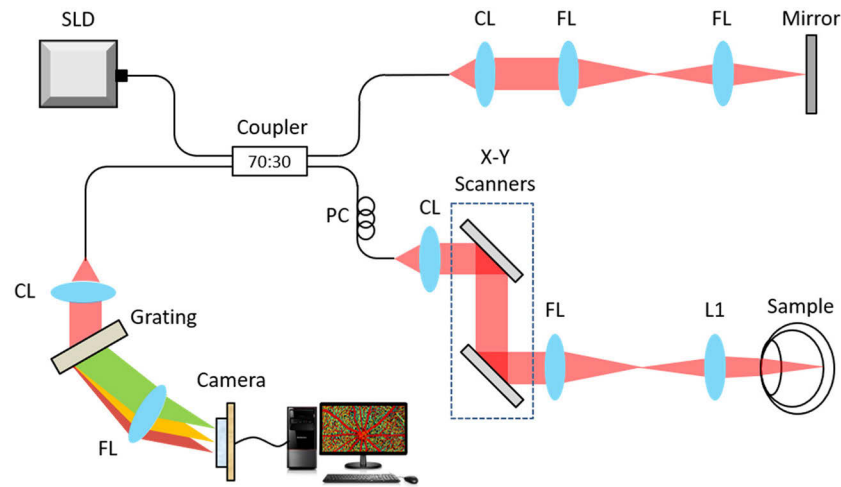


**Fig. 1.** Schematic of the OCT system setup. SLD: super luminescent diode; CL: collimate lens; FL: focus lens; PC: polarization controller; L1: ocular lens.

mice were anesthetized by intraperitoneal injection of 1% pentobarbital (0.01 ml/g body weight) and fixed in a custom-designed animal holder to minimize movements caused by heartbeat and breathing. The pupil was dilated with 2% tropicamide and 2% phenylephrine hydrochloride. During the entire experiments, the room temperature was controlled at ~25 centigrade and a heating pad was used to maintain the animals' body temperature so as to suppress the influence of temperature fluctuations on OAC [21]. All OCTA scans were conducted before noon in order to minimize diurnal variation. The whole-blood sample was taken from the tail immediately after the OCTA scan for each mouse, and its BCG was measured with a portable blood glucose meter (OneTouch Ultra, Johnson & Johnson, USA). All animal experimental procedures in this study were approved by the Animal Care and Use Committee of Zhejiang University.

### 2.3. Data processing

Several pretreatment steps and motion contrast OCTA algorithm were applied to effectively extract the dynamic blood signals within the mouse retina. Fourier transform of the raw spectral signal  $S(k, x, y, t)$  along the wavenumber  $k$  dimension was performed to generate the depth ( $z$ ) resolved reflectivity profile  $A(z, x, y, t)$ , where  $x$  is the fast scan direction,  $y$  is the slow scan direction, and  $t$  is the temporal index of the repeated B-scans at the same position. The structural cross-sectional image (Fig. 2(a)) was generated by the amplitude component of  $A$ . A cross-correlation registration algorithm was performed to compensate the eye movement between repeated B-frames, and then the OCTA motion contrast was computed using the inter-frame complex decorrelation with a local kernel [22]. Furthermore, to suppress the random noise-induced decorrelation artifacts, a signal-to-noise ratio (SNR) adaptive vascular mask was generated by combining the features of inverse SNR and decorrelation (ID) and applied on the decorrelation mapping, generating the final OCT angiograms (ID-OCTA) [19].

Due to the optical scattering and absorption of tissue, OCT probe light is attenuated as the beam penetrates into tissue. At the 840 nm wavelength band, because the attenuation is mainly caused by tissue scattering [13], local scattering coefficient can be calculated based on the OCT depth profile. Before calculating OAC, following procedures were applied to suppress disturbances introduced by depth-dependent signal decay and the noise of OCT system [12]:

$$I[i] = \frac{I_{origin}[i] - N[i]}{S[i]}, \quad (1)$$

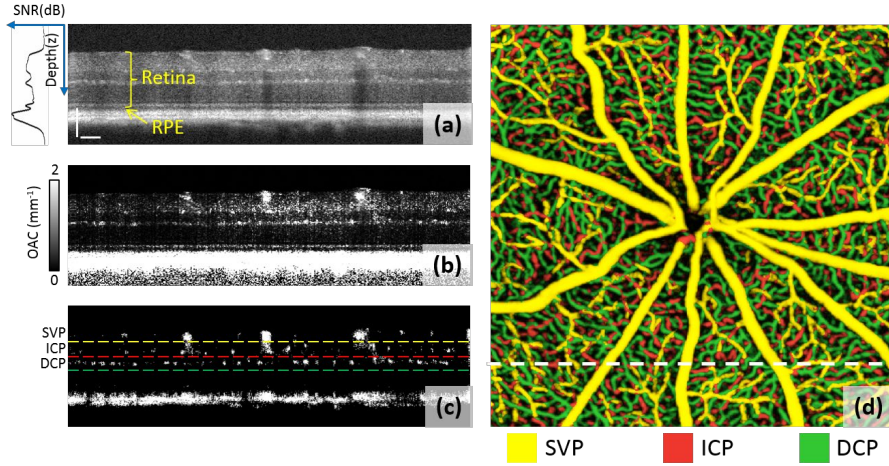


**Fig. 2.** Representative structural and vascular images of mouse retina in vivo. Structural (a), OAC (b) and angiographic (c) cross-sections, and the insert in (a) is the average depth profile. (d) The depth-encoded en face ID-OCTA angiogram. RPE: retinal pigment epithelium layer; SVP: superficial vessel plexus; ICP: intermediate capillary plexus; DCP: deep capillary plexus. The white dashed line in (d) indicates the location of the cross-section in (a-c). Scale bars shown in (a) correspond to 100  $\mu\text{m}$  and also apply to (b-d).

where  $I_{\text{origin}}[i]$  denotes the origin OCT signal intensity of the  $i^{\text{th}}$  pixel along the A-line.  $N[i]$  is the background noise acquired by blocking the sample arm and averaging a large number of A-lines. A sinc function ( $S[i] = \text{sinc}(\sigma i)$ ) was used to model the signal decay, where  $\sigma$  was determined by sensitivity roll-off measurement. Then, based on the calibrated data  $I[i]$ , the localized per-pixel OAC was calculated as follows [12]:

$$\mu[i] = \frac{I[i]}{2\Delta \sum_{i+1}^{\infty} I[i]}, \quad (2)$$

where  $\mu[i]$  denotes the OAC of the  $i^{\text{th}}$  pixel along the A-line, and  $\Delta$  refers to the pixel size in the depth direction. Thus, a depth-resolved OAC mapping of retina can be obtained (see Fig. 2(b)).

In order to analyze the OAC distribution corresponding to specific regions of retina, the OCTA vascular image was binarized with a linear ID threshold, generating a vascular mask [23]. Overlapping the vascular mask with the corresponding OAC matrix, the OAC distribution of vascular regions was acquired. According to the architecture of murine retinal microvasculature, blood vessels can be segmented into three layers: the superficial vessel plexus (SVP) in the ganglion cell layer, the intermediate capillary plexus (ICP) in the inner plexiform layer, and the deep capillary plexus (DCP) in the outer plexiform layer [24]. Based on the inverse-mask, the OAC distribution of background tissues (BT) can also be obtained. For further analysis, the total retina (TR) was divided into three sub-parts: BT, small vessels (SV) and arteries & veins (AR & VE), where SV means all retinal vessels except AR and VE. AR and VE were differentiated empirically based on their morphological differences in the en face OCTA image, that is, arteries are thinner with more branches, while veins are thicker with less branches [25]. In this paper, it is worth noting that the parts used to calculate the mean OAC values of BT and TR were the retinal regions above the upper boundary of retinal pigment epithelium (RPE) layer as indicated by the yellow bracket in Fig. 2(a).

#### 2.4. Statistical analysis

The correlation between OAC and BGC was linearly fitted based on the least squares criterion, and the correlation coefficient  $R$  was calculated. Differences in OAC values between control and DB groups were characterized through Student  $t$ -test, and it was considered to be statistically significant when  $P < 0.05$ .

### 3. Results

The cross-sectional image revealed the depth-resolved backscattering of different cellular and extracellular tissue constituents in mouse retina (see Fig. 2(a)). The OCT depth profile (the left curve in Fig. 2(a)) revealed the decay of the received OCT signal along the depth direction, and the depth-resolved OAC ( $\mu$ ) was computed to measure the intensity attenuation against depth (see Fig. 2(b)). The ID-OCTA angiogram was generated by analyzing the temporal dynamics of OCT signals (see Fig. 2(c)), and the 3D vasculature can be readily differentiated from the surrounding tissues (see Fig. 2(d)).

Utilizing the 3D vasculature generated by ID-OCTA, TR was divided into three sub-parts: BT, SV and AR & VE. The projectional OAC mappings of TR (Fig. 3(a)), BT (Fig. 3(b)), SV (Fig. 3(c)) and AR & VE (Fig. 3(d)) were generated by averaging the corresponding 3D OAC values in the depth direction. Generally, the retinal OAC of DB mouse is higher than that of normal mouse. The OAC values were further averaged over the x-y plane and plotted over the corresponding BGC values (Column #3 in Fig. 3) for each mouse. The averaged OAC ( $\mu$ ) of TR, BT, SV, AR and VE were linearly fitted to the measured BGCs ( $G$ ) with the following equations:  $\mu_{TR} = 4.72 \cdot 10^{-4} \cdot G + 0.60$ ,  $\mu_{BT} = 3.58 \cdot 10^{-4} \cdot G + 0.50$ ,  $\mu_{SV} = 2.73 \cdot 10^{-3} \cdot G + 2.64$ ,  $\mu_{AR} = 6.89 \cdot 10^{-3} \cdot G + 3.45$  and  $\mu_{VE} = 5.36 \cdot 10^{-3} \cdot G + 2.84$ , respectively. In addition, statistical analysis was performed between the control and DB groups. The BGC levels of DB group ( $438 \pm 53$  mg/dL) are significantly ( $P < 0.001$ ) higher than those of control group ( $150 \pm 40$  mg/dL), and elevated OAC levels were observed in all the retinal sub-parts of the DB group (Column #4 in Fig. 3). Generally, the blood components presented a more reliable OAC-BGC correlation than the background tissues, in terms of both the correlation coefficient  $R$  and the statistical significance  $P$ . Furthermore, different kinds of vessels also presented different performances. Both the AR (Fig. 3(d4)) and VE (Fig. 3(d6)) presented a significant ( $P < 0.001$ ) increase of OAC in the DB group, and the VE had a higher correlation coefficient ( $R=0.86$ ) between the measured OAC and BGCs (Fig. 3(d5)) than that of the AR ( $R=0.73$ ). The AR and VE presented a OAC change of  $\sim 0.07 \text{ mm}^{-1}$  per 10 mg/dl and  $\sim 0.05 \text{ mm}^{-1}$  per 10 mg/dl, respectively. It's worth noting that, in the early stage, the DB mouse retina (Fig. 3(e2)) presented no obvious change of vascular morphology in comparison with the control (Fig. 3(e1)) group. Thus, the OCTA enabled a vessel-specific assessment of the blood OAC which had a tight correlation to the BGC and a significant difference of blood OAC between the control and DB groups in mouse retina was observed.



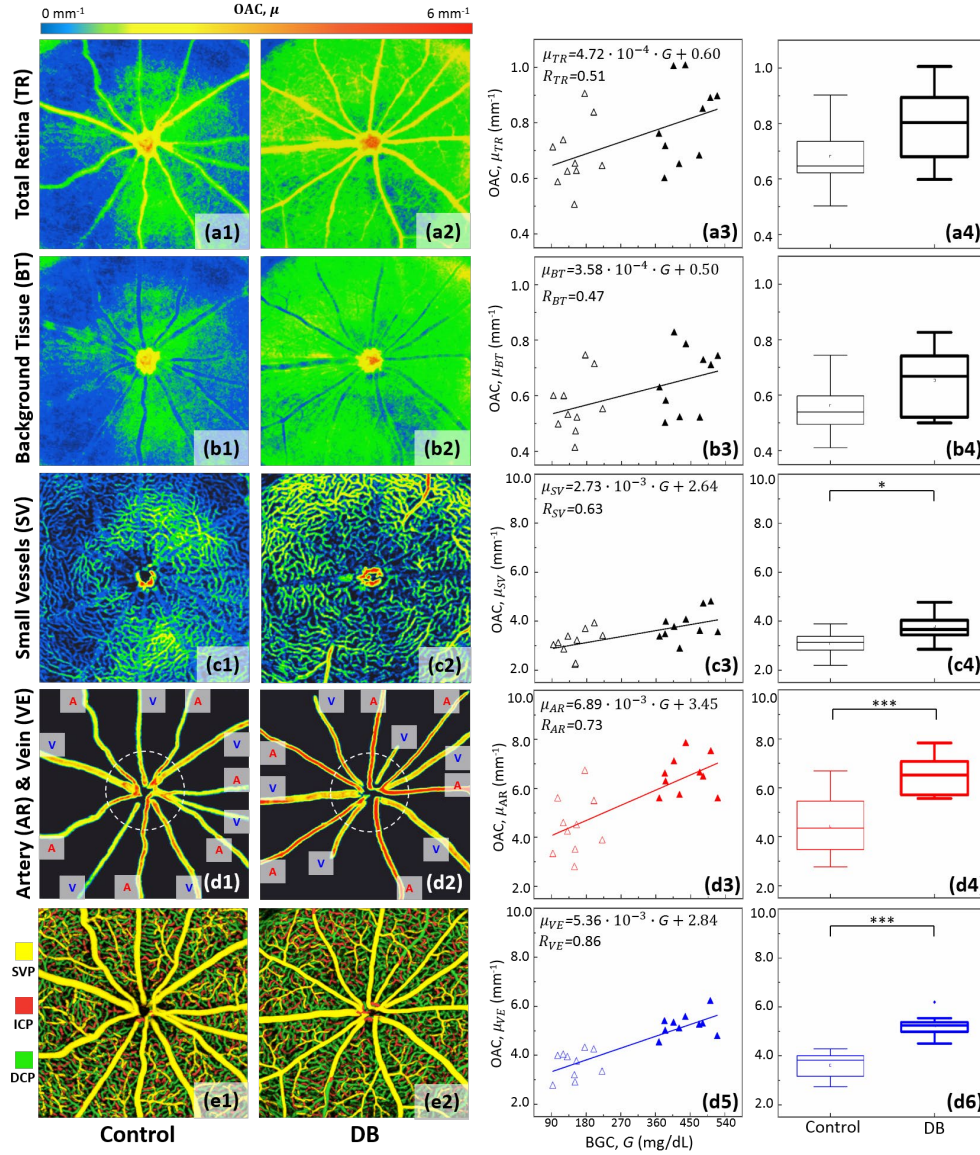


**Fig. 3.** OCTA-based OAC measurement and its relation to BGC in mouse retina. (a) total retina (TR), (b) background tissue (BT), (c) small vessels (SV), and (d) arteries & veins (AR & VE). SV means all retinal vessels except AR & VE. Representative projectional OAC mappings of control (Column #1 in a-d) and DB (Column #2 in a-d) groups. (Column #3 in a-d) Scatterplots of OAC versus BGC of each subject in the control (hollow triangle,  $n = 10$ ) and DB (solid triangle,  $n = 10$ ) groups. Solid lines are the linear fitting curves. (Column #4 in a-d) Boxplots of OAC in the control (thin) and DB (bold) groups. The arteries and veins in (d1) and (d2) were marked by A and V, respectively. Representative depth-encoded en face angiograms of normal (e1) and DB (e2) retina. The FOV (x-y) of OCTA imaging is 2 mm  $\times$  2 mm. BGC was measured with a glucose analyzer. \*\*\* indicates  $P < 0.001$ , and \* indicates  $P < 0.05$ .

#### 4. Discussion

In the conventional OCT-G, the skin OAC was measured for monitoring the blood glucose [13]. Because of the heterogeneity of the lower dermis, the OCT-G is highly sensitive to the tissue motion [13], while the blood is much homogeneous and has a high OAC-Glucose relation in vitro [16]. Inspired by these evidences, we proposed a OCTA-based blood OAC measurement. In the method, the 3D vasculature was obtained with ID-OCTA, and the blood OAC of specific vessels was measured in vivo by analyzing the OCT depth profile. It was found that the blood OAC was closely correlated to the BGC and a significant difference of OAC exists between the control and DB groups in mouse retina. Accordingly, the blood OAC-BGC correlation suggests a non-invasive OCTA-G, allowing a vessel-specific assessment of the blood glucose with improved motion immunity.

The physical and physiological mechanisms of the proposed OCTA-G is different from that of the conventional OCT-G. Compared with the changes in tissue absorption induced by glucose as chromophore, the observed changes of BGC-dependent OAC are mainly caused by the changes in tissue scattering attributed to glucose as osmolyte [13]. In the conventional OCT-G, the tissue scattering is mainly influenced by the RI mismatch between the interstitial fluid and cell membranes, and it decreases as the increased glucose concentration reduces the RI mismatch [14]. Thus, the OCT-G is a measurement of the interstitial glucose [26]. Comparatively, in addition to affecting the RI of plasma, the increase of blood glucose also increases the plasma osmolarity and deforms the shape of erythrocyte, resulting in the change of the complex RI of erythrocyte and the blood scattering [27,28]. A linear correlation between the osmolarity (225 to 400 mosmol/L) and the erythrocyte OAC in saline solution has been reported [29]. The influence of the glucose concentration on the RI of plasma and the effect of glucose osmolarity on the optical scattering of the erythrocyte was evaluated with a theoretical model, which demonstrated the administration of 5000 mg/dl glucose solution into the blood plasma increased the blood OAC  $\sim 0.06 \text{ mm}^{-1}$  per 10 mg/dl at the wavelength of 1000 nm [28]. Thus, the osmolarity-induced RI change of the erythrocyte should be the main origin of the observed increase of blood OAC, and thus the OCTA-G would be a measurement of the blood glucose. As we know, the arterial and venous blood glucose differs from the interstitial glucose level in the process of the glucose transport [5,26].

The accuracy of our OAC measurement and the observed OAC-BGC correlation agree well with related literatures. The nerve fiber layer (NFL) was measured with a OAC of  $2.19 \pm 0.34 \text{ mm}^{-1}$  in mouse retina (data not shown), which is close to the reported  $2.40 \pm 0.80 \text{ mm}^{-1}$  in the NFL of human retina [30]. The fresh blood sample of mouse was reported with a BGC of  $\sim 229 \text{ mg/dl}$  and a OAC of  $\sim 6 \text{ mm}^{-1}$  [16], and our linear fitting predicted similar OACs of  $5.03 \text{ mm}^{-1}$  (AR) and  $4.07 \text{ mm}^{-1}$  (VE) at the corresponding BGC level (Fig. 3(d)). In addition, the AR and VE presented a OAC change of  $\sim 0.05\text{-}0.07 \text{ mm}^{-1}$  per 10 mg/dl at the BGC range of  $\sim 90\text{-}520 \text{ mg/dl}$  in the mouse retina in vivo, and the diluted blood samples reported a OAC change of  $\sim 0.13 \text{ mm}^{-1}$  per 10 mg/dl at the BGC range of 20-287 mg/dl in vitro [16], which is a little higher than our measurement in vivo. It's worth noting that distinct from the acute erythrocytic change by directly injecting glucose to the blood samples in most available literatures [16,28], the change of the blood OAC in our study is the result of a chronic erythrocytic change caused by DB disease.

The limitation of the proposed OCTA-G is that the blood OAC measurement is substance unspecific. As shown in Fig. 3(d), the arteries presented an averaged  $1.04 \text{ mm}^{-1}$  elevation of the blood OAC relative to the veins, which corresponds to a BGC difference of 208 mg/dl according to the fitting equation. Although the glucose level in the arterial blood is higher than the glucose traveling back through the veins at any given time [5,26], the calculated BGC difference between arteries and veins is totally beyond the physiological range in mice ( $\sim 10 \text{ mg/dl}$ ) [31]. In addition to the difference of BGC, the oxygen saturation also contributed to the blood OAC differences between the arteries and veins, and it had a larger influence on the scattering than absorption

[32]. Besides, the blood OAC is also affected by the factors such as free fatty acid concentration, hematocrit and ionic concentration [13,32,33]. Thus, the blood OAC of the similar kind of vessels was preferred for assessing the BGC level.

Distinct from the decreased OAC of the lower dermis with respect to the increased BGC, both the OAC of the total retina and the background tissue increased as the BGC grows. The increased glucose concentration would change the osmolarity of the interstitial fluid, and subsequently changes the RI and the morphology of the neurocytes in retina [34]. Additionally, unlike the optically opaque skin tissue, the retina is almost optically transparent and the RIs of neighboring retinal layers were nearly uniform [35], and an increase of the glucose concentration might enlarge the RI mismatch in the retina. Considering the weak correlation ( $R=0.47$  and  $0.51$ ) between the tissue OAC and the BGC, there might be a complicated mechanism which deserves further studies in the future.

As a common microvascular complication of DB, diabetic retinopathy (DR) is a major cause of vision loss in middle-aged and elderly people, and the hyperglycaemia is one of the most consistent risk factors for the development of DR. Nevertheless, in clinical practice, a proportion of DB patients with poor glycaemia control do not develop DR, while that with appropriate control develop severe stages of DR [36–38]. The local BGC of the retina might have a closer relation to the DR development than that of the fingertip, but the direct and longitudinal monitoring of retinal BGC is hardly achieved by taking blood samples for chemical analysis. The proposed OCTA-G can be readily applied to the commercial ophthalmic OCT, and the averaged blood OAC of specific vessels facilitates a rapid and long-term monitoring of the retinal BGC with superior motion immunity.

**Funding.** National Natural Science Foundation of China (62075189); Natural Science Foundation of Zhejiang Province (LR19F050002); Zhejiang Lab (2018EB0ZX01); Hebei Key Laboratory of Micro-Nano Precision Optical Sensing and Measurement Technology (NEUQ202104).

**Disclosures.** The authors declare no conflicts of interest.

**Data Availability.** Data underlying the results presented in this paper are not publicly available at this time but may be obtained from the authors upon reasonable request. Correspondence should be addressed to the corresponding author.

## References

1. S. Wild, G. Roglic, A. Green, R. Sicree, and H. King, "Global prevalence of diabetes - estimates for the year 2000 and projections for 2030," *Diabetes Care* **27**(5), 1047–1053 (2004).
2. D. Daneman, "Type 1 diabetes," *Lancet* **367**(9513), 847–858 (2006).
3. International Diabetes Federation, "*IDF Diabetes Atlas, 9th edn*," (International Diabetes Federation, Brussels, 2020).
4. D. C. Klonoff, "Noninvasive Blood Glucose Monitoring," *Diabetes Care* **20**(3), 433–437 (1997).
5. M. Shokrehodaie and S. Quinones, "Review of non-invasive glucose sensing techniques: optical, electrical and breath acetone," *Sensors* **20**(5), 1251 (2020).
6. P. John, N. J. Vasa, S. N. Unni, and S. R. Rao, "Glucose sensing in oral mucosa simulating phantom using differential absorption based frequency domain low-coherence interferometry," *Appl. Opt.* **56**(29), 8257–8265 (2017).
7. M. Kohl, M. Cope, M. Essenpreis, and D. Bocker, "Influence of glucose-concentration on light-scattering in tissue-simulating phantoms," *Opt. Lett.* **19**(24), 2170–2172 (1994).
8. J. S. Maier, S. A. Walker, S. Fantini, M. A. Franceschini, and E. Gratton, "Possible correlation between blood-glucose concentration and the reduced scattering coefficient of tissues in the near-infrared," *Opt. Lett.* **19**(24), 2062–2064 (1994).
9. D. Huang, E. A. Swanson, C. P. Lin, J. S. Schuman, W. G. Stinson, W. Chang, M. R. Hee, T. Flotte, K. Gregory, C. A. Puliafito, and J. G. Fujimoto, "Optical coherence tomography," *Science* **254**(5035), 1178–1181 (1991).
10. D. J. Faber, F. J. v. d. Meer, M. C. G. Aalders, and T. G. v. Leeuwen, "Quantitative measurement of attenuation coefficients of weakly scattering media using optical coherence tomography," *Opt. Express* **12**(19), 4353–4365 (2004).
11. S. S. Yang, K. Z. Liu, H. J. Ding, H. Gao, X. X. Zheng, Z. H. Ding, K. D. Xu, and P. Li, "Longitudinal in vivo intrinsic optical imaging of cortical blood perfusion and tissue damage in focal photothrombosis stroke model," *J. Cereb. Blood Flow Metab.* **39**(7), 1381–1393 (2019).
12. K. A. Vermeer, J. Mo, J. J. A. Weda, H. G. Lemij, and J. F. de Boer, "Depth-resolved model-based reconstruction of attenuation coefficients in optical coherence tomography," *Biomed. Opt. Express* **5**(1), 322–337 (2014).
13. K. V. Larin, M. Motamedi, T. V. Ashitkov, and R. O. Esenaliev, "Specificity of noninvasive blood glucose sensing using optical coherence tomography technique: a pilot study," *Phys. Med. Biol.* **48**(10), 1371–1390 (2003).



14. R. O. Esenaliev, K. V. Larin, I. V. Larina, and M. Motamedi, "Noninvasive monitoring of glucose concentration with optical coherence tomography," *Opt. Lett.* **26**(13), 992–994 (2001).
15. K. V. Larin, M. S. Eledrisi, M. Motamedi, and R. O. Esenaliev, "Noninvasive blood glucose monitoring with optical coherence tomography," *Diabetes Care* **25**(12), 2263–2267 (2002).
16. L. R. De Pretto, T. M. Yoshimura, M. S. Ribeiro, and A. Z. de Freitas, "Optical coherence tomography for blood glucose monitoring in vitro through spatial and temporal approaches," *J. Biomed. Opt.* **21**(8), 086007 (2016).
17. R. K. Wang, S. L. Jacques, Z. Ma, S. Hurst, S. R. Hanson, and A. Gruber, "Three dimensional optical angiography," *Opt. Express* **15**(7), 4083–4097 (2007).
18. Y. Jia, O. Tan, J. Tokayer, B. Potsaid, Y. Wang, J. J. Liu, M. F. Kraus, H. Subhash, J. G. Fujimoto, J. Hornegger, and D. Huang, "Split-spectrum amplitude-decorrelation angiography with optical coherence tomography," *Opt. Express* **20**(4), 4710–4725 (2012).
19. L. Z. Huang, Y. M. Fu, R. X. Chen, S. S. Yang, H. X. Qiu, X. N. Wu, S. Y. Zhao, Y. Gu, and P. Li, "SNR-adaptive OCT angiography enabled by statistical characterization of intensity and decorrelation with multi-variate time series model," *IEEE Trans. Med. Imaging* **38**(11), 2695–2704 (2019).
20. H. K. Li, K. Y. Liu, L. Yao, X. F. Deng, Z. Y. Zhang, and P. Li, "ID-OCTA: OCT angiography based on inverse SNR and decorrelation features," *J. Innov. Opt. Health Sci.* **14**(01), 2130001 (2021).
21. Y. Su, X. S. Yao, Z. H. Li, Z. Meng, T. G. Liu, and L. Z. Wang, "Measurements of the thermal coefficient of optical attenuation at different depth regions of in vivo human skins using optical coherence tomography: a pilot study," *Biomed. Opt. Express* **6**(2), 500–513 (2015).
22. L. Guo, P. Li, C. Pan, R. J. Liao, Y. X. Cheng, W. W. Hu, Z. Chen, Z. H. Ding, and P. Li, "Improved motion contrast and processing efficiency in OCT angiography using complex-correlation algorithm," *J. Opt.* **18**(2), 025301 (2016).
23. Y. Zhang, H. Li, T. Cao, R. Chen, H. Qiu, Y. Gu, and P. Li, "Automatic 3D adaptive vessel segmentation based on linear relationship between intensity and complex-decorrelation in optical coherence tomography angiography," *Quant. Imaging Med. Surg.* **11**(3), 895–906 (2020).
24. M. Paques, R. Tadayoni, R. Sercombe, P. Laurent, O. Genevois, A. Gaudric, and E. Vicaut, "Structural and hemodynamic analysis of the mouse retinal microcirculation," *Invest. Ophthalmol. Vis. Sci.* **44**(11), 4960–4967 (2003).
25. T.-H. Kim, D. Le, T. Son, and X. Yao, "Vascular morphology and blood flow signatures for differential artery-vein analysis in optical coherence tomography of the retina," *Invest. Ophthalmol. Visual Sci.* **12**(1), 367–379 (2021).
26. E. Cengiz and W. V. Tamborlane, "A tale of two compartments: interstitial versus blood glucose monitoring," *Diabetes Technol. Ther.* **11**(S1), S-11–S-16 (2009).
27. M. Kinnunen, A. Kauppila, A. Karmenyan, and R. Myllyla, "Effect of the size and shape of a red blood cell on elastic light scattering properties at the single-cell level," *Invest. Ophthalmol. Visual Sci.* **2**(7), 1803–1814 (2011).
28. D. M. Zhestkov, A. N. Bashkatov, E. A. Genina, and V. V. Tuchin, "Influence of clearing solutions osmolarity on the optical properties of RBC," in *Saratov Fall Meeting 2003: Optical Technologies in Biophysics and Medicine V* (SPIE, 2004), pp. 321–330.
29. M. Friebe, J. Helfmann, and M. C. Meinke, "Influence of osmolarity on the optical properties of human erythrocytes," *J. Biomed. Opt.* **15**(5), 055005 (2010).
30. F. Visser, K. A. Vermeer, B. Ghafaryasl, A. M. M. Vlaar, V. Apostolov, J. v. H. Hubar, H. C. Weinstein, J. F. de Boer, and H. W. Berendse, "In vivo exploration of retinal nerve fiber layer morphology in Parkinson's disease patients," *J. Neural Transm.* **125**(6), 931–936 (2018).
31. A. Tahara, Y. Kondo, T. Takasu, and H. Tomiyama, "Effects of the SGLT2 inhibitor ipragliflozin on food intake, appetite-regulating hormones, and arteriovenous differences in postprandial glucose levels in type 2 diabetic rats," *Biomed. Pharmacother.* **105**, 1033–1041 (2018).
32. N. Bosschaart, G. J. Edelman, M. C. G. Aalders, T. G. van Leeuwen, and D. J. Faber, "A literature review and novel theoretical approach on the optical properties of whole blood," *Lasers Med. Sci.* **29**(2), 453–479 (2014).
33. K. Zirk and H. Poetzsckhe, "On the suitability of refractometry for the analysis of glucose in blood-derived fluids," *Med. Eng. Phys.* **26**(6), 473–481 (2004).
34. C. Pfäffle, H. Spahr, L. Kutzner, S. Burhan, F. Hilge, Y. Miura, G. Hüttmann, and D. Hillmann, "Simultaneous functional imaging of neuronal and photoreceptor layers in living human retina," *Opt. Lett.* **44**(23), 5671–5674 (2019).
35. E. P. Chen, "Refractive-indices of the rat retinal layers," *Ophthalmic Res.* **25**(1), 65–68 (1993).
36. H. A. Keenan, T. Costacou, J. K. Sun, A. Doria, J. Cavallerano, J. Coney, T. J. Orchard, L. P. Aiello, and G. L. King, "Clinical factors associated with resistance to microvascular complications in diabetic patients of extreme disease duration - The 50-year medalist study," *Diabetes Care* **30**(8), 1995–1997 (2007).
37. L. Y. Zhang, G. Krzentowski, A. Albert, and P. J. Lefebvre, "Risk of developing retinopathy in diabetes control and complications trial type 1 diabetic patients with good or poor metabolic control," *Diabetes Care* **24**(7), 1275–1279 (2001).
38. T. Y. Wong, C. M. G. Cheung, M. Larsen, S. Sharma, and R. Simo, "Diabetic retinopathy," *Nat. Rev. Dis. Primers* **2**(1), 16012 (2016).